Zinc-Doped BiOBr Hollow Microspheres for Enhanced Visible Light Photocatalytic Degradation of Antibiotic Residues

Yao Tang, Ran Tai, Xingjian Song, Shuai Gao, Runjie Wu, Shaowei Chen,* Peishen Li, and Qiang Wang*

Cite This: *Langmuir* 2024, 40, 6515−6523
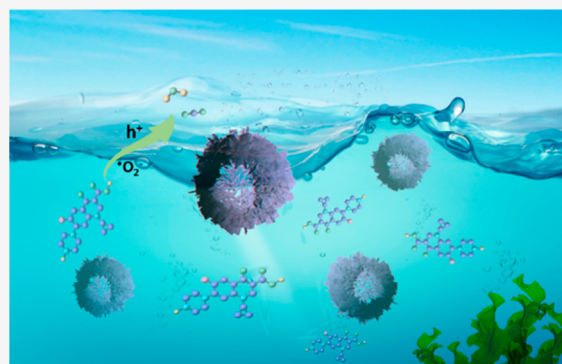
Read Online

| ACCESS | | Metrics & More | | Article Recommendations | | Supporting Information |

ABSTRACT: Photocatalysis represents an effective technology for environmental remediation. Herein, a series of Zn-doped BiOBr hollow microspheres are synthesized via one-pot solvothermal treatment of bismuth nitrate and dodecyl ammonium bromide in ethylene glycol along with a calculated amount of zinc acetate. Whereas the materials morphology and crystal structure remain virtually unchanged upon Zn-doping, the photocatalytic performance toward the degradation of ciprofloxacin is significantly improved under visible light irradiation. This is due to the formation of a unique band structure that facilitates the separation of photogenerated electron−hole pairs, reduced electron-transfer resistance, and enhanced electron mobility and carrier concentration. The best sample consists of a Zn doping amount of 1%, which leads to a 99.2% degradation rate of ciprofloxacin under visible photoirradiation for 30 min. The resulting photocatalysts also exhibit good stability and reusability, and the degradation intermediates exhibit reduced cytotoxicity compared to ciprofloxacin. These results highlight the unique potential of BiOBr-based photocatalysts for environmental remediation.
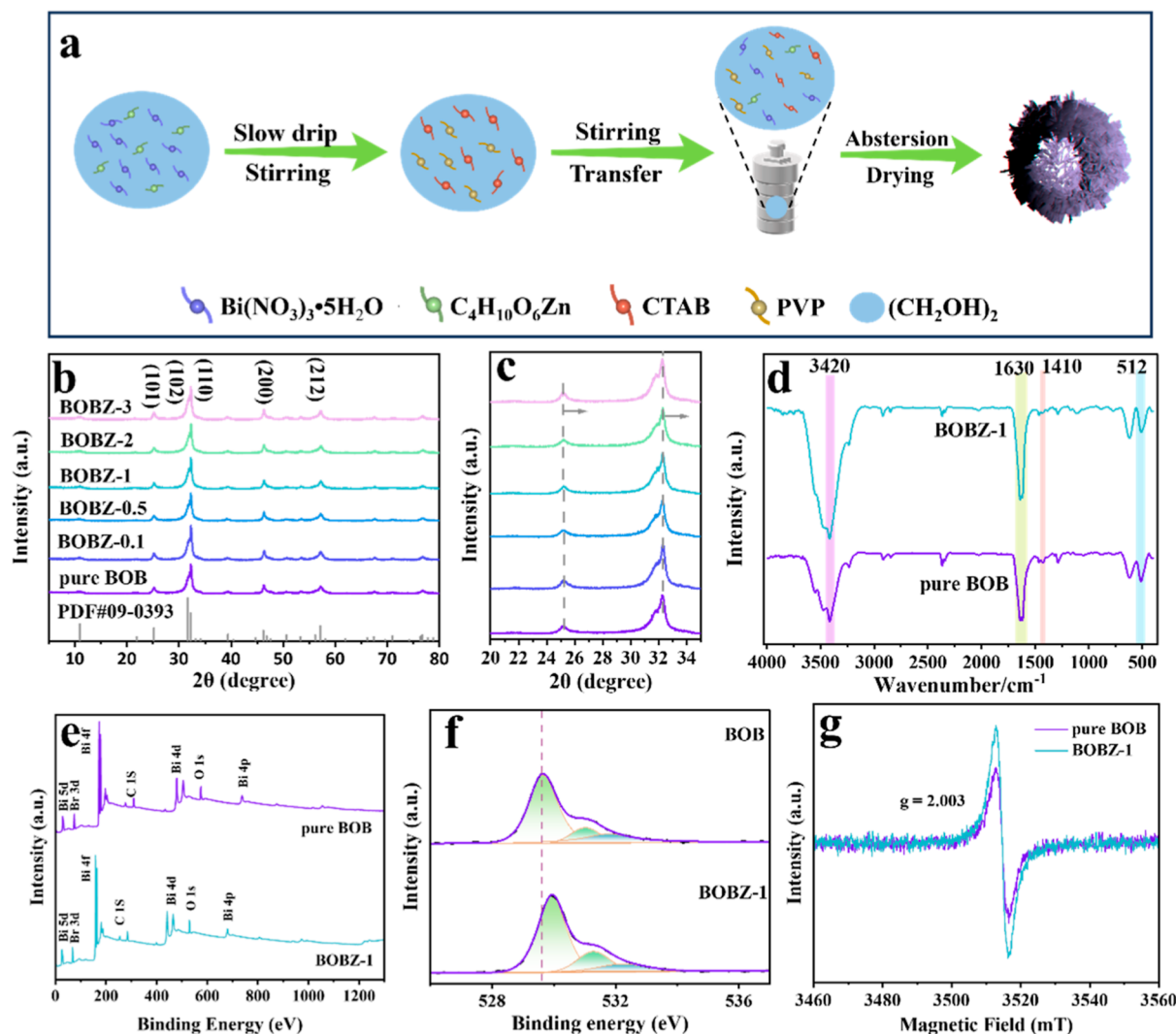

1. INTRODUCTION

Antibiotics have played a pivotal and revolutionary role in the history of human progress, with a profound impact on the fields of medicine, public health, and human longevity.[1,2] Nevertheless, the misuse and overreliance on antibiotics pose significant threats to both human health and the environment, contributing to the escalation of bacterial resistance and contamination of aquatic ecosystems upon entry into water bodies.[3−6] Therefore, removal of antibiotic residues in water is an important part of maintaining ecological balance and protecting human health.[7,8] Due to its multiple advantages such as high efficiency, environmental friendliness, and broad spectrum application, photocatalytic degradation stands out among the many technologies to remove antibiotics in water and has become the main tool of antibiotic degradation.[9−11] However, the limited spectral response range, low photo-electric conversion efficiency, and high electron−hole recombination rate of conventional semiconductor photo-catalysts limit the development of photocatalytic degradation technology. Many methods, such as morphology control, surface modification, and heterogeneous structure design, have been used to mitigate these issues and improve the performance and sustainable application.[12−16]

Among these, BiOBr possesses an appropriate band gap, excellent responsiveness to visible light, and remarkable environmental friendliness.[17,18] Consequently, they have emerged as a prominent semiconductor material within the realm of photocatalysis. However, the common issues of semiconductor materials still limit the application of BiOBr.[19−22] It is well-known that inorganic nanomaterials with a hollow structure may possess excellent optical properties, good loading and wrapping capability, high dispersion, and cyclic stability and thus have attracted wide attention. For instance, Liu et al.[23] synthesized multilayered porous TiO₂ hollow microspheres by a one-step template method and used them for rhodamine B degradation, with an efficiency far superior to that of commercial P25. Wang et al.[24] synthesized C-doped ZnO by a solvothermal method, which was 8.9 and 10.5 times more active than nano-ZnO in degrading organic pollutants and splitting water, respectively.

The photocatalytic performance can be further improved by deliberate doping of select heteroatoms into the semi-conductor materials. This is due to the regulation of the band structure of the semiconductor that enhances the separation and transport of photogenerated charges, leading

Figure 1. (a) Schematic illustration of the procedure of sample synthesis. (b) XRD patterns of the sample series, with the low-angle region magnified in panel (c). (d) FTIR spectra, (e) XPS survey spectra, (f) high-resolution scans of the O 1s electrons and (g) ESR spectra of pure BOB and BOBZ-1.

to improved overall activity and stability of the catalyst. For instance, Yu et al.[25] prepared Zn-doped CuO_2 particles via a solvothermal method and observed an enhanced photoelectron and hole separation efficiency of the CuO_2 particles, leading to a 94.6% degradation rate of ciprofloxacin (CIP, a commonly used antibiotic). Savunthari et al.[26] incorporated Zn into BaO_2 and SrO_2 to degrade rhodamine B and observed degradation rates of 99.9 and 99.8% within 15 and 10 min, respectively.

In this study, Zn-doped BiOBr hollow microspheres were prepared via a one-pot solvothermal method using ethylene glycol as the solvent and bismuth nitrate and dodecyl ammonium bromide as the precursors, along with the addition of a controlled amount of zinc acetate. Among the series, BiOBr doped with 1% Zn dopants stood out as the best photocatalyst for the degradation of CIP, reaching a degradation efficiency of 99.2% under visible photoirradiation for 30 min due to its unique band structure, low electron-transfer resistance, and high electron mobility and carrier concentration. In conjunction with the results from the free radical quenching experiment and electron spin resonance (ESR) analysis, the mechanism of the degradation of CIP was revealed.

2. EXPERIMENTAL SECTION

2.1. Chemicals. Zinc acetate $(Zn(CH_3COO)_2)$, bismuth nitrate pentahydrate $(Bi(NO_3)_3 \cdot 5H_2O)$, ethylene glycol $(C_2H_6O_2)$, dodecyl ammonium bromide (DDAB), polyvinylpyrrolidone (PVP), ethanol (CH_3CH_2OH), benzoquinone (BQ), oxalate (AO), isopropyl alcohol (IPA), sodium chloride (NaCl), sodium carbonate (Na_2CO_3), and sodium sulfate (Na_2SO_4) were purchased from McLean Biochemistry. All chemicals were of analytical grade and used in their as-received form without further purification. Deionized water was used throughout the study.

2.2. Sample Preparation. The synthetic procedure of the samples is schematically illustrated in Figure 1a. In a typical reaction, 1.944 g of $Bi(NO_3)_3 \cdot 5H_2O$ was dissolved into 25 mL of ethylene glycol, along with a calculated amount of zinc acetate dihydrate (at concentrations of 0, 0.1, 0.5, 1, 2, and 3%). Separately, 1.457 g of DDAB and 0.05 g of PVP were dispersed into 25 mL of ethylene glycol under magnetic stirring for 1 h. The first solution was added slowly into the second solution under stirring for 30 min, and the resulting mixture was transferred to a 100 mL stainless steel autoclave lined with polytetrafluoroethylene, which was heated at 120 °C for 10 h. The obtained samples were washed with deionized water and ethanol for three times and dried at 80 °C for 6 h and denoted as pure BOB, BOBZ-0.1, BOBZ-0.5, BOBZ-1, BOBZ-2, and BOBZ-3, respectively.
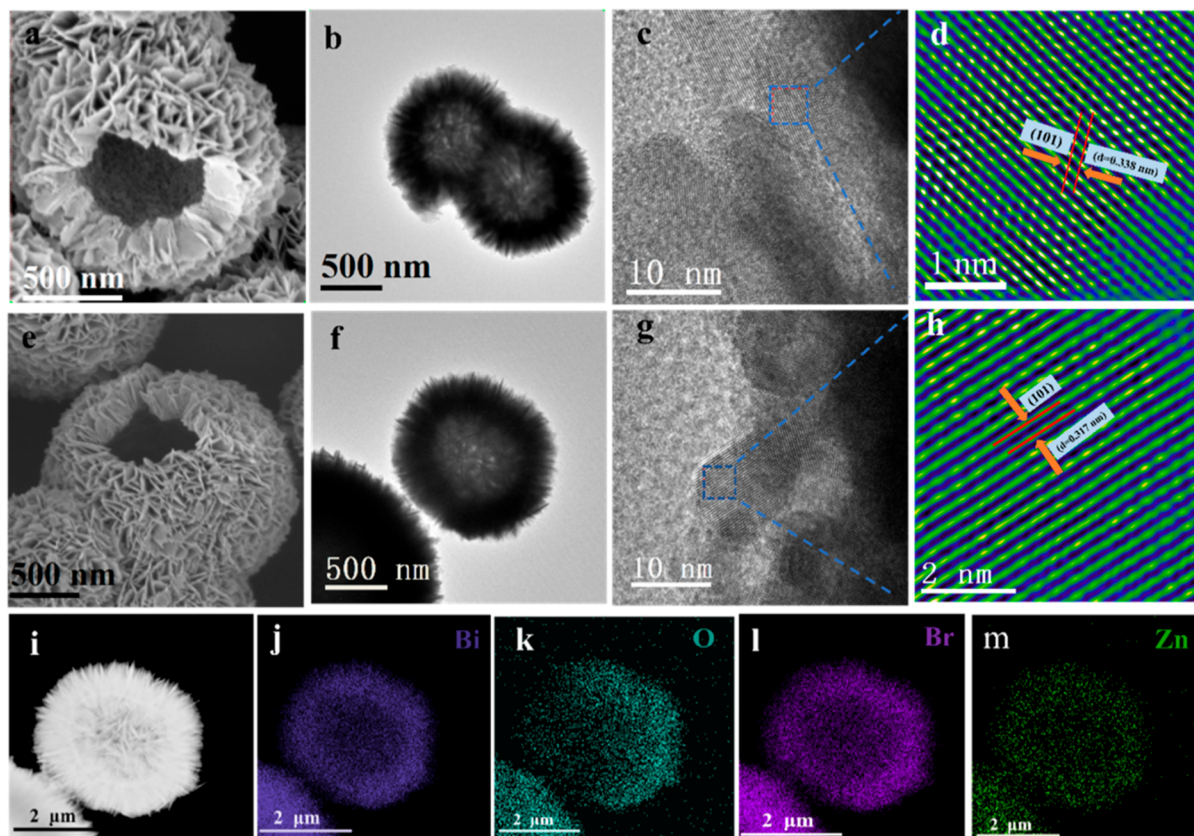
Figure 2. (a,e) SEM, (b,f) TEM, and (c,g) HRTEM images of (a−c) pure BOB and (e−g) BOBZ-1. (d,h) IFFT images of the selected areas in (c,g). (i−m) EDS-based elemental maps of BOBZ-1.

2.3. Structural Characterizations. Scanning electron microscopy (SEM) analysis was performed with a Hitachi S-4800 microscope, whereas transmission electron microscopy (TEM) measurements were carried out with a JEM-2010 electron microscope, which was also equipped with an energy-dispersive X-ray spectroscopy (EDS) accessary. X-ray diffraction (XRD) patterns were acquired with a Shimadzu X-ray diffractometer (SHIMADZU XRD-6100) using Cu Kα radiation. Fourier-transformed infrared (FTIR) measurements were carried out with a Bruker spectrometer by pressing the samples into KBr pellets. X-ray photoelectron spectroscopy (XPS) studies were conducted with a Thermo Kratos Axis Supra instrument, where the binding energy was calibrated against the C 1s peak at 284.8 eV. UV−vis spectroscopy measurements were conducted with a Thermo UV-2600 spectrophotometer. Electrochemical studies were performed with a CHI 760E Electrochemical Workstation by using a saturated calomel electrode (SCE) as the reference electrode. Photoluminescence (PL) profiles were obtained with an Edinburgh FLS9 fluorescence spectrometer. ESR spectra were collected with a Bruker ER200-SRC-10/12 spectrometer using 5,5-dimethyl-1-pyrrolidene-n-oxide (DMPO) and 2,2,6,6-tetramethylpiperidine n-oxide (TEMPO) as the $\bullet O_2^-$ and h$^+$ traps, respectively. Liquid chromatography−mass spectrometry (LC−MS) measurements were carried out with a Thermo Scientific Q Exactive/Focus LC−MS/MS/Ultimate 3000 UPLC. Nitrogen sorption measurements were performed with a Mike ASAP2020 instrument.

2.4. Photocatalytic Degradation. For the photocatalytic degradation of CIP, 10 mg of the (undoped and Zn-doped) BiOBr samples prepared above was dispersed into 50 mL of a CIP solution (10 mg L^{-1}). The mixture was allowed to achieve an adsorption equilibrium in the dark for 30 min before being exposed to visible light irradiation with simulated sunlight. Subsequently, an aliquot (2 mL) of the reaction solution was extracted at 5 min intervals. The catalyst was separated via centrifugation, and the absorbance of CIP at 272 nm was measured using a UV−vis spectrophotometer.

3. RESULTS AND DISCUSSION

3.1. Sample Structural Characterizations. The sample structure was first examined by XRD measurements. From the XRD patterns in Figure 1b, both (undoped) BOB and (Zn-doped) BOBZ can be seen to exhibit four diffraction peaks at 2θ = 25.6, 46.26, 57.07, and 31.68°. These peaks align well with the tetragonal phase of BiOBr (JCPDS card no. 09-0393), indicating that Zn doping, even up to 3%, did not induce marked alterations of the crystalline structure of BiOBr.[27] Yet, with the increase of Zn doping, the diffraction peaks can be seen to shift to a slightly higher angle (Figure 1c), likely because part of the Bi^{3+} in the BiOBr matrix were replaced by smaller Zn^{2+} (atomic radius r = 0.103 and 0.074 nm, respectively).[28] Consistent results were obtained in FTIR measurements (Figure 1d), where pure BOB and BOBZ-1 exhibited a similar spectrum, featuring two vibrational bands at 3420 and 1630 cm^{-1} due to the tensile and bending vibrations of free water O−H, respectively,[29] and two additional bands at 1410 and 512 cm^{-1} arising from the asymmetric stretching of the Bi−Br bond and the symmetric stretching vibration of the Bi−O bond, respectively.[30]

The elemental composition and valence states of the samples were subsequently probed by XPS measurements. From the survey spectra presented in Figure 1e, the elements of Bi, Br, and O can be distinctly identified in both pure BOB and BOBZ-1 samples. Notably, the Zn signals of BOBZ-1 were below the detection limit of the instrument (Figure S1a).[25] Figure S1b shows the high-resolution scan of the Bi 4f electrons, where the Bi $4f_{7/2}/4f_{5/2}$ doublet can be resolved at 158.91/164.18 eV for pure BOB and blue-shifted slightly to
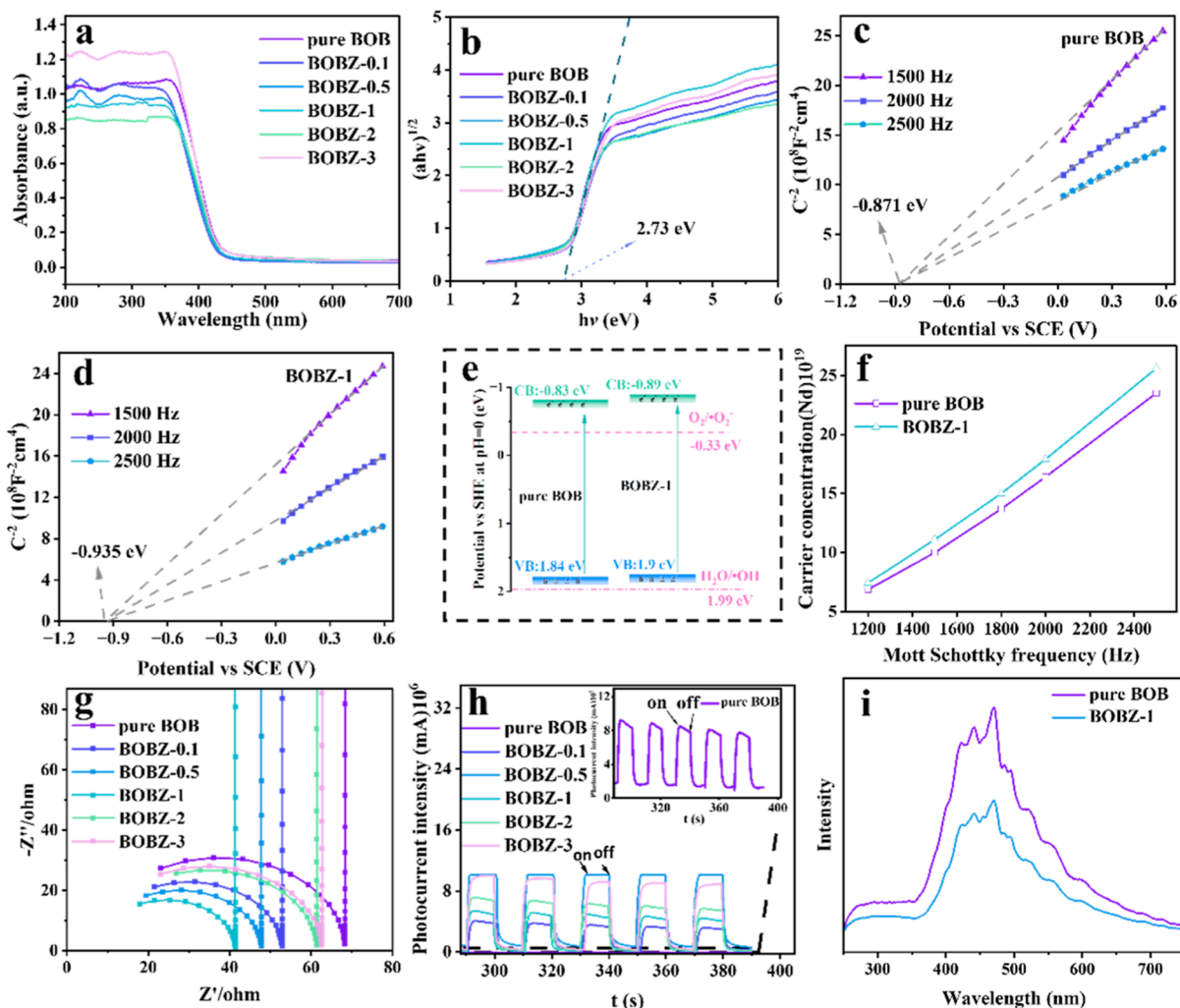
Figure 3. (a) DRS spectra and (b) Tauc plots of the sample series. M−S profiles of (c) pure BOB and (d) BOBZ-1 at 1500, 2000, and 2500 Hz. (e) Electronic band diagrams and (f) carrier concentrations of pure BOB and BOBZ-1. (g) Nyquist plots and (h) transient photocurrent profiles of the sample series. Inset to panel (h) is the zoom in of the response profile of pure BOB. (i) PL emission spectra of pure BOB and BOBZ-1.

159.10/164.42 eV for BOBZ-1, suggesting electron depletion of Bi^{3+} due to Zn doping.[31] The Br 3d spectra are shown in Figure S1c, which entailed a doublet at 68.14/69.10 eV for pure BOB and 68.15/69.19 eV for BOBZ-1.[32] From the O 1s spectra (Figure 1f), three subpeaks can be deconvoluted at 529.60, 531.10, and 531.91 eV for BOB and blue-shifted slightly to 529.91, 531.27, and 532.25 eV for BOBZ-1 due to lattice oxygen (Bi−O), surface oxygen, and hydroxyl oxygen (O−H), respectively.[33] It can be seen that the binding energies of BOBZ-1 all have a slight blue shift compared to those of pure BOB, most likely due to the change of chemical environment caused by the incorporation of Zn dopants.[34] In addition, ESR measurements (Figure 1g) suggest the formation of oxygen vacancies in both pure BOB and BOBZ-1, and the concentration increases with increasing Zn doping.[35] Such defects played a critical role in enhancing the photocatalytic performance toward CIP degradation, as manifested below.[36,37]

Further structural insights were garnered through SEM measurements. From Figure 2a, the pure BOB can be seen to feature a 3D hollow microsphere structure with the shells made of smooth 2D nanosheets. Such a structure can also be observed with BOBZ-1 (Figure 2e), indicating minimal

impacts of Zn doping on the sample morphology. Consistent findings were obtained in TEM measurements, as illustrated in Figure 2b,f. Notably, in high-resolution TEM analyses, well-defined lattice fringes can be readily resolved (Figure 2c,g). The inverse fast Fourier transform (IFFT) patterns are shown in Figure 2d,h, where BOB featured an interplanar spacing of 0.338 nm, consistent with the (101) crystal faces of BiOBr.[38] By contrast, BOBZ-1 exhibited a somewhat smaller interplanar spacing of 0.317 nm, suggesting a shrinking lattice due to Zn doping, which is consistent with the above XRD results. In addition, EDS-based elemental mapping analysis (Figure 2i− m) showed that the elements of Bi, O, Br, and Zn were uniformly distributed on the surface of BOBZ-1.

In N_2 adsorption−desorption measurements, both pure BOB and BOBZ-1 exhibited a type IV isotherm (Figure S1d and inset), indicating the formation of a mesoporous structure, and the specific surface area was estimated to be 23.30 cm^3 g^{-1} for BOB and somewhat lower at 17.15 cm^3 g^{-1} for BOBZ-1.

3.2. Photo Absorption and Photoelectrochemical Analysis. The band structures of the samples were then evaluated by UV−vis diffuse reflectance spectroscopy (DRS) measurements and Mott−Schottky (M−S) analysis.[16,39] Figure 3a shows the DRS spectra of pure BOB and the series of
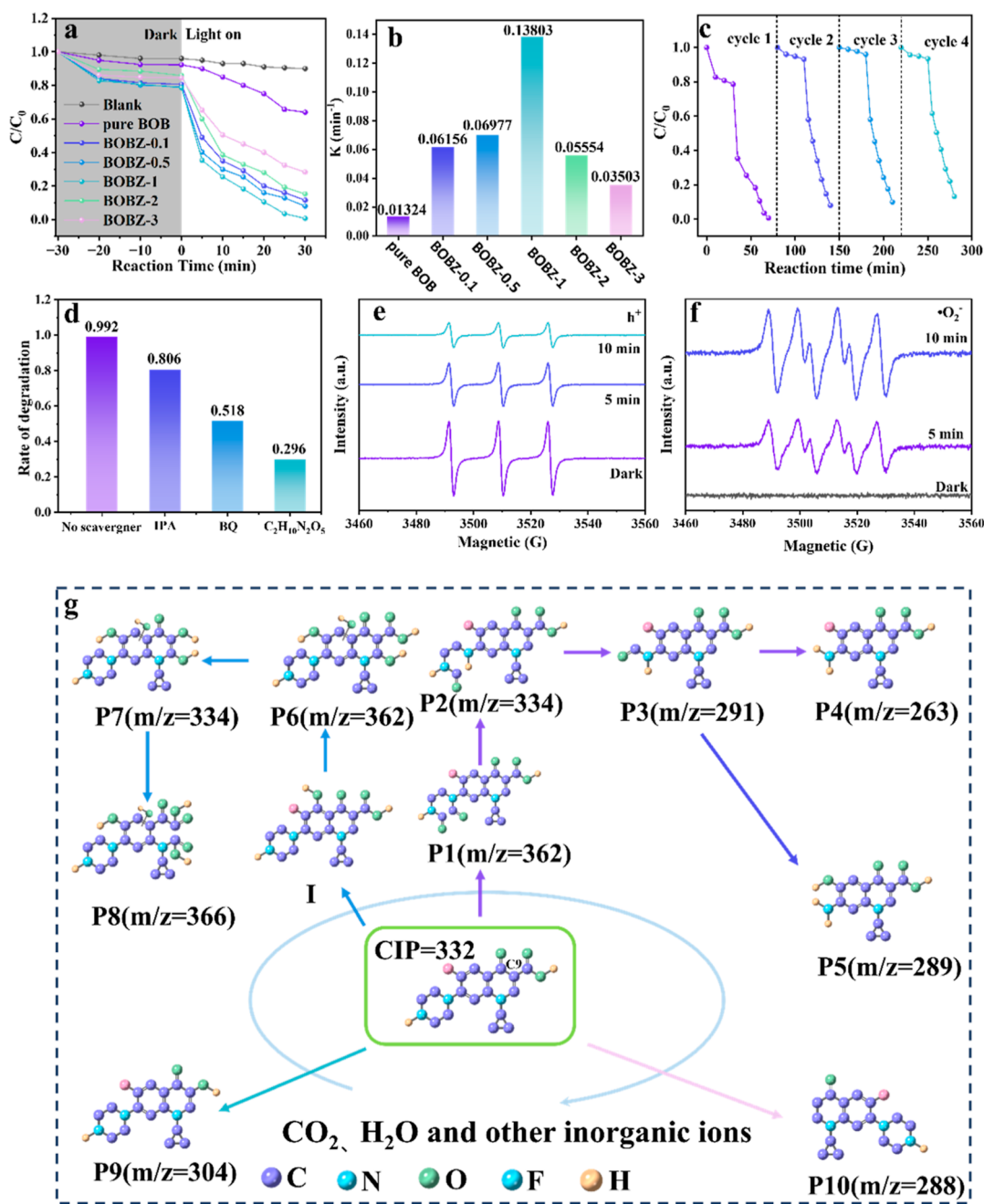
Figure 4. (a) Photocatalytic degradation of CIP by pure BOB and BOBZ samples under visible light irradiation for up to 30 min. (b) Pseudo-first-order rate constants of CIP degradation by the sample series. (c) Four cycles of the photocatalytic degradation of CIP by BOBZ-1. (d) Efficacy of CIP degradation by BOBZ-1 in the absence and presence of various radical scavengers. ESR spectra of (e) TEMPO-h$^+$ and (f) DMPO-$^\bullet$O$_2^-$. (g) Possible photodegradation pathways of CIP with BOBZ-1.

BOBZ samples, which exhibit an almost identical absorption edge at 454 nm. From the corresponding Tauc plots (Figure 3b), the band gap (E_g) was estimated to be ca. 2.73 eV. The M−S profiles at 1500, 2000, and 2500 Hz for pure BOB and BOBZ-1 are depicted in Figure 3c,d, respectively. Both samples can be seen to exhibit a positive slope, indicative of N-type semiconductors.[40] In addition, from the x-axis intercepts of −0.871 and −0.935 eV, the flat-band potentials can be calculated to be −0.63 and −0.69 eV relative to the SCE reference. For N-type semiconductors, their flat band potential is 0.2 eV positive compared to the conduction band (CB) potential.[41] Therefore, the CB minimum for pure BOB and BOBZ-1 is determined to be −0.83 and −0.89 eV, respectively,

and the corresponding valence band (VB) maximum is ca. 1.9 eV for BOB and 1.84 eV for BOBZ-1. The resulting band structure diagrams are shown in Figure 3e.

The carrier density (N_d) of the samples was subsequently determined from the slope of the M−S diagram using the formula, $N_d = \dfrac{2}{e^0 \varepsilon \varepsilon_0} \left[\dfrac{d \frac{1}{C^2}}{dV} \right]^{-1}$, where e^0 is the electronic charge (1.6×10^{-19} C), ε is the dielectric constant of BiOBr ($\varepsilon = 4.7$ F m^{-1}), ε_0 is the vacuum permittivity (8.86×10^{-12} F m^{-1}), and V is the applied bias at the electrode. From Figure 3f, one can see that BOBZ-1 possessed an apparently higher carrier concentration than pure BOB within the frequency range of

1200−2400 Hz (other frequency data are shown in Figure S2a,b).[42] Figure 3g depicts the Nyquist plots of the sample series, where BOBZ-1 can be seen to display the lowest electron-transfer resistance (R_{CT}). The corresponding photocurrent profiles are shown in Figure 3h and inset, where visible photoirradiation led to a marked increase of the sample current and BOBZ-1 exhibited the highest current response among the series, BOBZ-1 > B0BZ-0.5 > BOBZ-0.1 > BOBZ-2 > BOBZ-3 > pure BOB. In PL measurements (Figure 3i), BOBZ-1 can be found to display a weaker emission than pure BOB, indicating a reduced recombination rate of photogenerated electrons and holes.[43] Taken together, these results show that among the sample series, BOBZ-1 exhibited the strongest photoelectric responses, the highest charge mobility, and the lowest electron-transfer resistance, which were conducive to a high photocatalytic performance toward the degradation of organic pollutants, as detailed below.

3.3. Photocatalytic Degradation of Ciprofloxacin. The photocatalytic activity of the sample series toward CIP degradation was then tested. Experimentally, 10 mg of the samples prepared above (Figure S1e) was dissolved in a CIP solution (10 mg L^{-1}, Figure S1f) at pH = 6.66 (Figure S1g). After an adsorption equilibrium in the dark for 30 min, the solution was exposed to visible light photoirradiation. From Figure 4a, it can be seen that in the absence of a photocatalyst, the self-degradation efficacy of CIP was under 10% at 30 min, whereas about 22% was degraded in the presence of pure BOB, and an even higher efficiency was observed with BOBZ. Notably, the degradation efficacy first increased with increasing Zn doping, reaching a maximum with BOBZ-1 (99.2%) and then diminishing with BOBZ-2 (70.2%) and BOBZ-3 (70.0%). This suggests that 1% Zn represented the best doping level.

Based on the quasi-first-order kinetics, the degradation rate was then estimated. From Figure 4b, it can be seen that BOBZ-1 possessed the highest reaction rate (k) of 0.138 min^{-1}, in comparison to 0.013 min^{-1} for BOB, 0.062 min^{-1} for BOBZ-0.1, 0.070 min^{-1} for BOBZ-0.5, 0.056 min^{-1} for BOBZ-2, and 0.035 min^{-1} for BOBZ-3.

In addition, as inorganic anions like Cl^{-}, SO$_4^{2-}$, and CO$_3^{2-}$ are commonly present in the actual water environment, their impacts on CIP degradation were also explored. From Figure S1h, one can see that such inorganic anions markedly inhibited the photocatalytic activity. This was likely because inorganic anions occupied part of the active sites on the composite catalysts, reacted with active groups, and/or acted as radical scavengers, resulting in reduced photocatalytic activity.[44,45] However, common cations in water (e.g., Na$^+$, K$^+$, Ca^{2+}, and NH$_4^+$) did not significantly impact the degradation of CIP (Figure S1i), possibly because these cations are chemically inert with the pollutants and photocatalysts.[46] The stability and recyclability of the photocatalysts were then tested by four cycles of CIP degradation with BOBZ-1.[47] From Figure 4c, it can be observed that the photocatalytic performance decreased by only ca. 8% after four cycles. This shows that the catalyst possessed a good cyclic stability. In fact, XRD and SEM measurements showed virtually no change of the crystal structure and morphology of BOBZ-1 after the tests (Figure S2c,d).

3.4. Degradation Pathways and Mechanism. Notably, when BQ[19] and oxalic acid (AO)[48] were added into the solution, the degradation efficiency of BOBZ-1 decreased significantly to only 51.8 and 29.6%, while the addition of IPA[49] produced only a small change (Figure 4d). As BQ, AO,

and IPA are the specific quenchers of h$^+$, $^{\bullet}$O$_2^{-}$, and $^{\bullet}$OH, respectively, this suggests that the degradation of CIP was mainly driven by h$^+$ and $^{\bullet}$O$_2^{-}$, with a minor contribution from $^{\bullet}$OH.

Consistent results were obtained from the ESR measurements. It can be seen from Figure 4e that the TEMPO signal gradually diminished with prolonged photoirradiation, due to the h$^+$ oxidation of TEMPO. This suggests effective production of h$^+$ under visible irradiation.[50] In addition, a sextet was observed, as shown in Figure 4f, due to the DMPO-$^{\bullet}$O$_2^{-}$ adduct, and the signals intensified with increasing photoirradiation time, indicative of enhanced $^{\bullet}$O$_2^{-}$ formation.

The organic intermediates produced during the catalytic degradation of CIP were then identified by LC−MS measurements. The chemical formula and residence time are listed in Table S1. Figure 4g shows the possible CIP degradation pathways. In path 1, the piperazine ring of CIP is oxidized, which leads to the opening of the ring structure and production of P1 (m/z = 362). P1 loses a CO, causing the piperazinyl ring to split and producing the ketone derivative P2 (m/z = 334), while the carbonyl group remains on the N of the alkyl amine. P2 loses an additional CO and an N and is further oxidized to produce intermediate P3 (m/z = 291). Further decarbonization of intermediate P3 leads to the formation of intermediate P4 (m/z = 263), and defluorination and rehydroxylation of P3 produces intermediate P5 (m/z = 289).[8,50] In path 2, the hydroxyl radical attacks C5 of CIP to produce intermediate I, which is unstable and rapidly transformed into P6 (m/z = 362), and further decarboxylated oxidation of P6 produces intermediate P7 (m/z = 334). In path 3, due to nucleophilic addition and $^{\bullet}$O$_2^{-}$ attack on quinolone groups, the fluoroquinolone decarboxylation in CIP yields an intermediate product P9 (m/z = 304).[51] In path 4, C9 in CIP is attacked by hydroxyl radicals, resulting in the decarboxylation to P10 (m/z = 288). Finally, P4, P5, P8, P9, and P10 are converted to water, carbon dioxide, and other inorganic ions by further oxidation.

The bioaccumulation factors and biotoxicity of CIP and intermediates in the degradation process were evaluated by the Toxicity assessment software (T.E.S.T.).[52] It is evident that most intermediates exhibit a low bioaccumulation factor value (Figure S2e). Notably, the developmental toxicity of most intermediates is also low (Figure S2f). In conclusion, BOBZ-1 can not only efficiently degrade CIP but also reduce its ecotoxicity. Therefore, the nanocomposite photocatalysts presented above can be exploited for the "green" removal of CIP from the aquatic environments.[53]

In addition, the mechanism of BOBZ-1 degradation of CIP was analyzed (Figure 5). Under photoirradiation, excited electrons and holes are formed on the BOBZ-1 surface. According to the energy band structure (Figure 3e), the CB of BOBZ-1 lies at −0.89 eV, which is more negative than the formal potential of oxygen reduction to $^{\bullet}$O$_2^{-}$ (−0.33 eV). Therefore, the photogenerated electrons can reduce the dissolved oxygen on the BOBZ-1 surface to $^{\bullet}$O$_2^{-}$. Although the holes that accumulate on the VB of BOBZ-1 do not possess an energy sufficiently high to oxidize OH^{-} or H$_2$O to produce $^{\bullet}$OH, they can induce the oxidation of CIP adsorbed on the catalyst surface into smaller, less harmful intermediates/products.[54] That is, both h$^+$ and $^{\bullet}$O$_2^{-}$ work collectively toward the degradation of CIP.
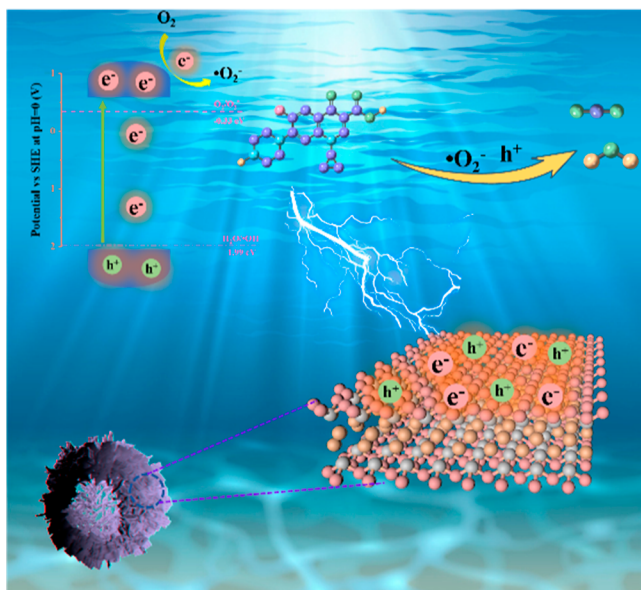
Figure 5. Mechanism of the photocatalytic degradation of CIP by BOBZ-1 under solar light irradiation.

4. CONCLUSIONS

In summary, Zn-doped BiOBr hollow spheres were successfully synthesized through a facile hydrothermal method and exhibited enhanced photocatalytic efficacy in the degradation of CIP, as compared to the undoped counterpart. Mechanistically, the incorporation of Zn dopants endowed BiOBr with a band structure that was conducive to the separation of photogenerated electron–hole pairs, leading to high carrier mobility and concentration and low electron-transfer resistance. This facilitated the reduction of dissolved oxygen to $^\bullet O_2^-$ radicals and the formation of h^+, both contributing to the oxidative degradation of CIP. Among the series, BOBZ-1 stood out as the best sample, removing 99.2% of CIP under visible light for 30 min, at a reaction rate of 0.138 min^{-1}, and most of the degradation intermediates were less toxic than CIP. Results from this work highlight the unique potential of BiOBr-based composites in the photocatalytic degradation of antibiotic pollutants in water.

ASSOCIATED CONTENT

ⓈI Supporting Information

The Supporting Information is available free of charge at https://pubs.acs.org/doi/10.1021/acs.langmuir.4c00155.

> Additional XPS scans of Zn 2p, Bi 4f, and Br 3d electrons of the samples; nitrogen sorption isotherms and pore size distribution; optimization of the experimental conditions for the photocatalytic degradation of CIP; theoretical simulations of the bioaccumulation factor and developmental toxicity of CIP degradation intermediates; and list of CIP degradation intermediates determined by LC–MS (PDF)

AUTHOR INFORMATION

Corresponding Authors

Shaowei Chen − *Department of Chemistry and Biochemistry, University of California, Santa Cruz, California 95064, United States;* ⓞ orcid.org/0000-0002-3668-8551; Email: shaowei@ucsc,.edu

Qiang Wang − *Laboratory for Micro-sized Functional Materials & College of Elementary Education and Department of Chemistry, Capital Normal University, Beijing 100048, China;* ⓞ orcid.org/0000-0002-9118-5615; Email: qwchem@gmail.com

Authors

Yao Tang − *Laboratory for Micro-sized Functional Materials & College of Elementary Education and Department of Chemistry, Capital Normal University, Beijing 100048, China*

Ran Tai − *Laboratory for Micro-sized Functional Materials & College of Elementary Education and Department of Chemistry, Capital Normal University, Beijing 100048, China*

Xingjian Song − *Department of Chemistry and Biochemistry, University of California, Santa Cruz, California 95064, United States*

Shuai Gao − *Laboratory for Micro-sized Functional Materials & College of Elementary Education and Department of Chemistry, Capital Normal University, Beijing 100048, China*

Runjie Wu − *Laboratory for Micro-sized Functional Materials & College of Elementary Education and Department of Chemistry, Capital Normal University, Beijing 100048, China*

Peishen Li − *College of Environmental Sciences and Engineering, The Key Laboratory of Water and Sediment Sciences (MOE), Peking University, Beijing 100871, China*

Complete contact information is available at:
https://pubs.acs.org/10.1021/acs.langmuir.4c00155

Author Contributions

The manuscript was written through contributions of all authors. All authors have given approval to the final version of the manuscript. These authors contributed equally.

Notes

The authors declare no competing financial interest.

■ REFERENCES

(1) Gil, J. Antimicrobial use in livestock farming. *Nat. Food* **2023**, *4* (2), 138.

(2) Yang, L.; Fan, D.; Li, Z.; Cheng, Y.; Yang, X.; Zhang, T. A Review on the Bioinspired Photocatalysts and Photocatalytic Systems. *Adv. Sustainable Syst.* **2022**, *6* (5), 2100477.

(3) Guo, F.; Zhang, H.; Li, H.; Shen, Z. Modulating the oxidative active species by regulating the valence of palladium cocatalyst in photocatalytic degradation of ciprofloxacin. *Appl. Catal., B* **2022**, *306*, 121092.

(4) Shi, X.; Li, Y.; Zhang, Z.; Sun, L.; Peng, Y. Enhancement of ciprofloxacin degradation in the Fe(II)/peroxymonosulfate system by protocatechuic acid over a wide initial pH range. *Chem. Eng. J.* **2019**, *372*, 1113−1121.

(5) Zhang, L.; Yue, Q.; Yang, K.; Zhao, P.; Gao, B. Enhanced phosphorus and ciprofloxacin removal in a modified BAF system by configuring Fe-C micro electrolysis: Investigation on pollutants removal and degradation mechanisms. *J. Hazard. Mater.* **2018**, *342*, 705−714.

(6) Arthur, R. B.; Bonin, J. L.; Ardill, L. P.; Rourk, E. J.; Patterson, H. H.; Stemmler, E. A. Photocatalytic degradation of ibuprofen over BiOCl nanosheets with identification of intermediates. *J. Hazard. Mater.* **2018**, *358*, 1–9.

(7) Zhang, X.; Kamali, M.; Xue, Y.; Li, S.; Costa, M. E. V.; Cabooter, D.; Dewil, R. Periodate activation with copper oxide nanomaterials for the degradation of ciprofloxacin - A new insight into the efficiency and mechanisms. *J. Cleaner Prod.* **2023**, *383*, 135412.

(8) Hu, X.; Hu, X.; Peng, Q.; Zhou, L.; Tan, X.; Jiang, L.; Tang, C.; Wang, H.; Liu, S.; Wang, Y.; Ning, Z. Mechanisms underlying the photocatalytic degradation pathway of ciprofloxacin with heterogeneous TiO_2. *Chem. Eng. J.* **2020**, *380*, 122366.

(9) Xu, H.; Zhang, Y.; Wang, Y.; Zhang, L.; Zhang, Z.; Zhong, L.; He, Z.; Zheng, Y.; Shen, Y. Heterojunction material $BiYO_3$/g-C_3N_4 modified with cellulose nanofibers for photocatalytic degradation of tetracycline. *Carbohydr. Polym.* **2023**, *312*, 120829.

(10) Xiong, X.; Wang, Z.; Zhang, Y.; Li, Z.; Shi, R.; Zhang, T. Wettability controlled photocatalytic reactive oxygen generation and Klebsiella pneumoniae inactivation over triphase systems. *Appl. Catal., B* **2020**, *264*, 118518.

(11) Tan, G.; Guo, Y. Q.; Zuo, L. Y.; Zhang, K.; Zhang, Y. M.; Zhang, L. L.; Yu, J. J.; Feng, X.; Li, B.; Wang, L. Y. Synthesis of zinc-based metal-organic framework as highly efficient photocatalyst for decomposition of organic dyes in aqueous solution. *Rare Met.* **2023**, *42* (4), 1205–1213.

(12) Diaz, N. O.; Rodríguez, C.; Durán-Álvarez, J. C.; Talreja, N.; Quispe-Fuentes, I.; Martínez-Avelar, C.; Bizarro, M.; Valdés, H.; Mera, A. C. A theoretical and experimental approach for photocatalytic degradation of caffeic acid using BiOBr microspheres. *Mater. Sci. Eng., B* **2021**, *273*, 115432.

(13) Qu, J.; Du, Y.; Ji, P.; Li, Z.; Jiang, N.; Sun, X.; Xue, L.; Li, H.; Sun, G. Fe, Cu co-doped BiOBr with improved photocatalytic ability of pollutants degradation. *J. Alloys Compd.* **2021**, *881*, 160391.

(14) Yu, Q.; Chen, J.; Li, Y.; Wen, M.; Liu, H.; Li, G.; An, T. In-situ decoration of metallic Bi on BiOBr with exposed (110) facets and surface oxygen vacancy for enhanced solar light photocatalytic degradation of gaseous n-hexane. *Chin. J. Catal.* **2020**, *41* (10), 1603–1612.

(15) Song, M.; Du, M.; Liu, Q.; Xing, F.; Huang, C.; Qiu, X. Enhancement of photocatalytic activities in hierarchical BiOBr microflowers induced by oxygen vacancies. *Catal. Today* **2019**, *335*, 193–199.

(16) Wang, Y.; Zhu, C.; Zuo, G.; Guo, Y.; Xiao, W.; Dai, Y.; Kong, J.; Xu, X.; Zhou, Y.; Xie, A.; Sun, C.; Xian, Q. 0D/2D Co_3O_4/TiO_2 Z-Scheme heterojunction for boosted photocatalytic degradation and mechanism investigation. *Appl. Catal., B* **2020**, *278*, 119298.

(17) He, Z.; Fareed, H.; Yang, H.; Xia, Y.; Su, J.; Wang, L.; Kang, L.; Wu, M.; Huang, Z. Mechanistic insight into the charge carrier separation and molecular oxygen activation of manganese doping BiOBr hollow microspheres. *J. Colloid Interface Sci.* **2023**, *629*, 355–367.

(18) He, Z.; Yang, H.; Sunarso, J.; Wong, N. H.; Huang, Z.; Xia, Y.; Wang, Y.; Su, J.; Wang, L.; Kang, L. Novel scheme towards interfacial charge transfer between $ZnIn_2S_4$ and BiOBr for efficient photocatalytic removal of organics and chromium (VI) from water. *Chemosphere* **2022**, *303*, 134973.

(19) Tang, Q. Y.; Yang, M. J.; Yang, S. Y.; Xu, Y. H. Enhanced photocatalytic degradation of glyphosate over 2D CoS/BiOBr heterojunctions under visible light irradiation. *J. Hazard. Mater.* **2021**, *407*, 124798.

(20) Jia, Y.; Liu, P.; Wang, Q.; Wu, Y.; Cao, D.; Qiao, Q. A. Construction of Bi_2S_3-BiOBr nanosheets on TiO_2 NTA as the effective photocatalysts: Pollutant removal, photoelectric conversion and hydrogen generation. *J. Colloid Interface Sci.* **2021**, *585*, 459–469.

(21) Gao, K.; Zhu, H.; Zhang, C.; Song, X.; Lao, L.; Ni, L.; Chen, J.; Cheng, C.; Wang, X. Boosting Photocatalytic Nitrogen Fixation via In Situ Constructing Bi Metal Active Sites over BiOBr/BiOI Heterojunction. *Sol. RRL* **2022**, *6* (12), 2200869.

(22) Sun, J.; Li, X.; Zhao, Q.; Liu, B. Ultrathin nanoflake-assembled hierarchical BiOBr microflower with highly exposed {001} facets for efficient photocatalytic degradation of gaseous ortho-dichlorobenzene. *Appl. Catal., B* **2021**, *281*, 119478.

(23) Liu, Z.; Bai, H.; Sun, D. Facile fabrication of hierarchical porous TiO_2 hollow microspheres with high photocatalytic activity for water purification. *Appl. Catal., B* **2011**, *104* (3–4), 234–238.

(24) Wang, S.; Zhang, X.; Li, S.; Fang, Y.; Pan, L.; Zou, J. J. C-doped ZnO ball-in-ball hollow microspheres for efficient photocatalytic and photoelectrochemical applications. *J. Hazard. Mater.* **2017**, *331*, 235–245.

(25) Yu, X.; Zhang, J.; Zhang, J.; Niu, J.; Zhao, J.; Wei, Y.; Yao, B. Photocatalytic degradation of ciprofloxacin using Zn-doped Cu_2O particles: Analysis of degradation pathways and intermediates. *Chem. Eng. J.* **2019**, *374*, 316–327.

(26) Savunthari, K. V.; Balaji, D.; Sudheer, N.; Bathwar, M.; Rangasamy, M.; Dhandabani, G. K.; Puente Santiago, A. R.; Shanmugam, S.; Kong, K. V.; R, V. Effective photocatalytic degradation of rhodamine-B over Zn-doped BaO2 and SrO2 composites under UV and sunlight irradiation. *RSC Sustain.* **2023**, *1*, 1511–1521.

(27) Shi, Y.; Li, J.; Huang, D.; Wang, X.; Huang, Y.; Chen, C.; Li, R. Specific Adsorption and Efficient Degradation of Cylindrospermopsin on Oxygen-Vacancy Sites of BiOBr. *ACS Catal.* **2023**, *13* (1), 445–458.

(28) Zhang, X.-B.; Zhang, L.; Hu, J. S.; Huang, X. H. Facile hydrothermal synthesis and improved photocatalytic activities of Zn^{2+} doped Bi_2MoO_6 nanosheets. *RSC Adv.* **2016**, *6* (38), 32349–32357.

(29) Wu, Y.; Ji, H.; Liu, Q.; Sun, Z.; Li, P.; Ding, P.; Guo, M.; Yi, X.; Xu, W.; Wang, C. C.; Gao, S.; Wang, Q.; Liu, W.; Chen, S. Visible light photocatalytic degradation of sulfanilamide enhanced by Mo doping of BiOBr nanoflowers. *J. Hazard. Mater.* **2022**, *424*, 127563.

(30) Meng, F.; Wang, J.; Tian, W.; Zhang, H.; Liu, S.; Tan, X.; Wang, S. Effects of inter/intralayer adsorption and direct/indirect reaction on photo-removal of pollutants by layered g-C_3N_4 and BiOBr. *J. Cleaner Prod.* **2021**, *322*, 129025.

(31) Shi, X.; Wang, P.; Li, W.; Bai, Y.; Xie, H.; Zhou, Y.; Ye, L. Change in photocatalytic NO removal mechanisms of ultrathin BiOBr/BiOI via NO_3^- adsorption. *Appl. Catal., B* **2019**, *243*, 322–329.

(32) Lv, X.; Yan, D. Y. S.; Lam, F. L. Y.; Ng, Y. H.; Yin, S.; An, A. K. Solvothermal synthesis of copper-doped BiOBr microflowers with enhanced adsorption and visible-light driven photocatalytic degradation of norfloxacin. *Chem. Eng. J.* **2020**, *401*, 126012.

(33) Hao, J.; Zhang, Y.; Zhang, L.; Shen, J.; Meng, L.; Wang, X. Restructuring surface frustrated Lewis acid-base pairs of BiOBr through isomorphous Sn doping for boosting photocatalytic CO_2 reduction. *Chem. Eng. J.* **2023**, *464*, 142536.

(34) Guan, C.; Hou, T.; Nie, W.; Zhang, Q.; Duan, L.; Zhao, X. Enhanced photocatalytic reduction of CO_2 on BiOBr under synergistic effect of Zn doping and induced oxygen vacancy generation. *J. Colloid Interface Sci.* **2023**, *633*, 177–188.

(35) Gao, S.; Ji, H.; Yang, P.; Guo, M.; Tressel, J.; Chen, S.; Wang, Q. High-Performance Photocatalytic Reduction of Nitrogen to Ammonia Driven by Oxygen Vacancy and Ferroelectric Polarization Field of $SrBi_4Ti_4O_{15}$ Nanosheets. *Small* **2023**, *19* (3), 2206114.

(36) Zou, X.; Sun, B.; Wang, L.; Bai, H.; Meng, X.; Li, C.; Li, Z. Enhanced photocatalytic degradation of tetracycline by SnS_2/Bi_2MoO_6-x heterojunction: Multi-electric field modulation through oxygen vacancies and Z-scheme charge transfer. *Chem. Eng. J.* **2024**, *482*, 148818.

(37) Liu, J.; Meng, C.; Zhang, X.; Wang, S.; Duan, K.; Li, X.; Hu, Y.; Cheng, H. Direct Z-scheme In_2O_3/AgI heterojunction with oxygen vacancies for efficient molecular oxygen activation and enhanced photocatalytic degradation of tetracycline. *Chem. Eng. J.* **2023**, *466*, 143319.

(38) Cai, M.; Shui, A.; Du, B. Constructing the ZnO/BiOBr hierarchical heterojunction for efficient pollutant photodegradation driven by visible-light. *Surf. Interfaces* **2023**, *37*, 102643.

(39) Li, K.; Ji, M.; Chen, R.; Jiang, Q.; Xia, J.; Li, H. Construction of nitrogen and phosphorus co-doped graphene quantum dots/Bi_5O_7I composites for accelerated charge separation and enhanced photocatalytic degradation performance. *Chin. J. Catal.* **2020**, *41* (8), 1230−1239.

(40) Li, W.; Wang, Z.; Li, Y.; Ghasemi, J. B.; Li, J.; Zhang, G. Visible-NIR light-responsive 0D/2D $CQDs/Sb_2WO_6$ nanosheets with enhanced photocatalytic degradation performance of RhB: Unveiling the dual roles of CQDs and mechanism study. *J. Hazard. Mater.* **2022**, *424*, 127595.

(41) Gou, N.; Yang, W.; Gao, S.; Li, Q. Incorporation of ultrathin porous metal-free graphite carbon nitride nanosheets in polyvinyl chloride for efficient photodegradation. *J. Hazard. Mater.* **2023**, *447*, 130795.

(42) Morgade, C. I. N.; Schvval, A. B.; Fuente, S. A.; Durán-Álvarez, J. C.; Buono, C.; Desimone, P. M.; Aldao, C. M.; Cabeza, G. F. Synthesis and Theoretical-Experimental Characterization of BiOBr: The Role of Oxygen and Halide Vacancies on the Optoelectric Properties of this Bismuth Oxyhalide. *Top. Catal.* **2022**, *65* (7−8), 824−838.

(43) He, Z.; Xia, Y.; Su, J.; Tang, B. Fabrication of magnetically separable $NiFe_2O_4/Bi_{24}O_{31}Br_{10}$ nanocomposites and excellent photocatalytic performance under visible light irradiation. *Opt. Mater.* **2019**, *88*, 195−203.

(44) Feng, C.; Lu, Z.; Zhang, Y.; Liang, Q.; Zhou, M.; Li, X.; Yao, C.; Li, Z.; Xu, S. A magnetically recyclable dual Z-scheme GCNQDs-$CoTiO_3/CoFe_2O_4$ composite photocatalyst for efficient photocatalytic degradation of oxytetracycline. *Chem. Eng. J.* **2022**, *435*, 134833.

(45) Li, J.; Xia, Z.; Ma, D.; Liu, G.; Song, N.; Xiang, D.; Xin, Y.; Zhang, G.; Chen, Q. Improving photocatalytic activity by construction of immobilized Z-scheme $CdS/Au/TiO_2$ nanobelt photocatalyst for eliminating norfloxacin from water. *J. Colloid Interface Sci.* **2021**, *586*, 243−256.

(46) Ding, P.; Ji, H.; Li, P.; Liu, Q.; Wu, Y.; Guo, M.; Zhou, Z.; Gao, S.; Xu, W.; Liu, W.; Wang, Q.; Chen, S. Visible-light degradation of antibiotics catalyzed by titania/zirconia/graphitic carbon nitride ternary nanocomposites: a combined experimental and theoretical study. *Appl. Catal., B* **2022**, *300*, 120633.

(47) Zhang, C.; Ouyang, Z.; Yang, Y.; Long, X.; Qin, L.; Wang, W.; Zhou, Y.; Qin, D.; Qin, F.; Lai, C. Molecular engineering of donor-acceptor structured $g-C_3N_4$ for superior photocatalytic oxytetracycline degradation. *Chem. Eng. J.* **2022**, *448*, 137370.

(48) Yang, Q.; Zhai, Y.; Xu, T.; Zhao, K.; Li, H. Facile fabrication of ScBiOBr photocatalyst immobilized on palm bark with enhanced visible light photocatalytic performance for estradiol degradation. *J. Phys. Chem. Solids* **2019**, *130*, 127−135.

(49) Chen, J.; Xiao, X.; Wang, Y.; Lu, M.; Zeng, X. Novel AgI/BiOBr/reduced graphene oxide Z-scheme photocatalytic system for efficient degradation of tetracycline. *J. Alloys Compd.* **2019**, *800*, 88−98.

(50) Hua, X.; Chen, H.; Rong, C.; Addison, F.; Dong, D.; Qu, J.; Liang, D.; Guo, Z.; Zheng, N.; Liu, H. Visible-light-driven photocatalytic degradation of tetracycline hydrochloride by Z-scheme $Ag_3PO_4/1T@2H-MoS_2$ heterojunction: Degradation mechanism, toxicity assessment, and potential applications. *J. Hazard. Mater.* **2023**, *448*, 130951.

(51) Jia, Z.; Li, T.; Zheng, Z.; Zhang, J.; Liu, J.; Li, R.; Wang, Y.; Zhang, X.; Wang, Y.; Fan, C. The BiOCl/diatomite composites for rapid photocatalytic degradation of ciprofloxacin: Efficiency, toxicity evaluation, mechanisms and pathways. *Chem. Eng. J.* **2020**, *380*, 122422.

(52) Yi, X. H.; Ji, H.; Wang, C. C.; Li, Y.; Li, Y. H.; Zhao, C.; Wang, A.; Fu, H.; Wang, P.; Zhao, X.; Liu, W. Photocatalysis-activated SR-AOP over PDINH/MIL-88A(Fe) composites for boosted chloroquine phosphate degradation: Performance, mechanism, pathway and DFT calculations. *Appl. Catal., B* **2021**, *293*, 120229.

(53) Wang, T.; Zhao, C.; Meng, L.; Li, Y.; Chu, H.; Wang, F.; Tao, Y.; Liu, W.; Wang, C. C. In-situ-construction of BiOI/UiO-66 heterostructure via nanoplate-on-octahedron: A novel p-n heterojunction photocatalyst for efficient sulfadiazine elimination. *Chem. Eng. J.* **2023**, *451*, 138624.

(54) He, Z.; Lin, K.; Hing Wong, N.; Sunarso, J.; Xia, Y.; Fu, X.; Su, J.; Huang, Z.; Wang, Y.; Tang, B. Elucidation of mechanisms, pathways, and toxicity of fabricated Z-scheme $KNbO_3/ZnIn_2S_4$ hollow core-shell composites for enhanced ciprofloxacin photodegradation. *Chem. Eng. J.* **2023**, *475*, 146262.